AIP | Review of Scientific Instruments

Higher order parametric excitation modes for spaceborne quadrupole mass spectrometers

D. J. Gershman, B. P. Block, M. Rubin, M. Benna, P. R. Mahaffy et al.

Citation: Rev. Sci. Instrum. **82**, 125109 (2011); doi: 10.1063/1.3669781
View online: http://dx.doi.org/10.1063/1.3669781
View Table of Contents: http://rsi.aip.org/resource/1/RSINAK/v82/i12
Published by the AIP Publishing LLC.

Higher order parametric excitation modes for spaceborne quadrupole mass spectrometers

D. J. Gershman,[1] B. P. Block,[1] M. Rubin,[1] M. Benna,[2] P. R. Mahaffy,[2] and T. H. Zurbuchen[1]
[1]*Department of Atmospheric, Oceanic and Space Sciences, University of Michigan, Ann Arbor, Michigan 48109, USA*
[2]*Solar Systems Exploration Division, NASA Goddard Space Flight Center, Greenbelt, Maryland 20771, USA*

(Received 25 July 2011; accepted 26 November 2011; published online 21 December 2011)

This paper describes a technique to significantly improve upon the mass peak shape and mass resolution of spaceborne quadrupole mass spectrometers (QMSs) through higher order auxiliary excitation of the quadrupole field. Using a novel multiresonant tank circuit, additional frequency components can be used to drive modulating voltages on the quadrupole rods in a practical manner, suitable for both improved commercial applications and spaceflight instruments. Auxiliary excitation at frequencies near twice that of the fundamental quadrupole RF frequency provides the advantages of previously studied parametric excitation techniques, but with the added benefit of increased sensed excitation amplitude dynamic range and the ability to operate voltage scan lines through the center of upper stability islands. Using a field programmable gate array, the amplitudes and frequencies of all QMS signals are digitally generated and managed, providing a robust and stable voltage control system. These techniques are experimentally verified through an interface with a commercial Pfeiffer QMG422 quadrupole rod system. When operating through the center of a stability island formed from higher order auxiliary excitation, approximately 50% and 400% improvements in 1% mass resolution and peak stability were measured, respectively, when compared with traditional QMS operation. Although tested with a circular rod system, the presented techniques have the potential to improve the performance of both circular and hyperbolic rod geometry QMS sensors. © *2011 American Institute of Physics*. [doi:10.1063/1.3669781]

I. INTRODUCTION

This paper describes a technique to significantly improve the performance of the spaceborne quadrupole mass spectrometer (QMS) through higher order auxiliary excitation of the quadrupole field. Through the invention of the quadrupole mass spectrometer in 1953, Paul and Steinwedel[1] unlocked the means to obtain unprecedented measurements of neutral gas composition and isotopic ratios. Since then, QMSs have revolutionized chemical analysis, by simultaneously reducing instrument mass, size, and cost, and increasing instrument scan speed when compared with traditional magnetic sector mass spectrometers.[2] Such advancements positioned QMS technology as the standard choice for low-energy spaceborne mass spectrometry applications. In fact, QMSs have flown on almost every mission to a planetary body in the solar system.[3–6] They have provided a set of ion and neutral composition data that has led to significant discoveries about planetary physics, chemistry, and composition, and have transformed the understanding of the origin of planetary atmospheres. (See, for example, Lunine,[7] and references therein.)

The specifications of an ideal measurement with a spaceborne QMS are three-fold. (1) The ability to distinguish between adjacent ion masses is set by the mass resolution, which must be large enough to achieve readable mass spectra. (2) Repeatable and predictable measured mass peak shapes are vital for the determination of precise isotopic ratios and relative abundance of different species. (3) Sensitivity, i.e. the successful transmission of desired particles through the instrument, must be high in order to measure species whose relative abundances span multiple orders of magnitude. Obtaining sufficient performance in these areas is especially challenging for space applications due to the power and mass constraints imposed on instrument design. However, improvements in all aspects of QMS operation are vital for the continued use of these highly successful instruments for the continued advancement of space and planetary science.

Over the last several years, the scientific objectives of solar system exploration have evolved, and with them, the requirements on space instrumentation. The emphasis of many previous missions has been on the measurement of low mass atoms and molecules (less than 100 amu) such as NH_3 and CH_4, and isotopic ratios, such as D/H or $^3He/^4He$, which provide insight into the origin of planetary bodies.[8–10] After having spent decades concentrating on solar system formation, the planetary community has shifted much of its focus to a new puzzle: what is the origin of life? The answer to this question requires the study of complex organics and volatiles in primitive bodies and planetary environments.[11] These molecules are both high in mass (100-1000 amu) and low in abundance, making them difficult to detect with current spaceborne QMS technology. In addition, noble gases and isotopic ratios in simple molecules are still of fundamental importance and have not yet been measured well in comets or on Venus. New QMS sensors must maintain the ability to make these measurements and at the same time be scalable to meet new science requirements. An order of magnitude improvement in both mass resolution (targeting $M/\Delta M \sim 10^3$) and abundance sensitivity (targeting the ppb range) will be re-

quired to detect and study these trace molecules, which may hold the key to understanding the potential for life in the solar system.

Similar QMS performance is desired in the commercial realm, which represents a much higher number of deployed sensors. Applications of this technology range from medical and biological analysis to forensic science.[12] These commercial spectrometers are typically lower-cost than their space-flight counterparts, and rely on the use of less expensive manufacturing and development processes that may lead to reductions in attainable instrument performance.[2] Any enhancement in the quality of QMS measurements has direct impact on both spaceborne and commercial QMS instruments, especially if this enhancement is achievable with relatively minor modifications. In fact, the improvements discussed in this paper are expected to be more profound for such commercial systems.

Parametric excitation of the quadrupole field is a technique that was originally implemented to mitigate the low mass side peak tail[13] that can occur as a consequence of using circular geometry, or from ions not spending sufficient time traversing the rods in order to be ejected. However, it has since been shown to provide improvement in maximum attainable mass resolution, improved quality of mass peak shapes, and, for higher resolution modes, increased instrument sensitivity.[14–18] In this approach, a second periodic signal drives the QMS rods at one of an ion trajectory's normal modes in order to hasten its ejection. However, parametric excitation techniques have previously[14,16] relied on methods that were rather inefficient in driving the quadrupole rods with auxiliary signals, limiting the maximum excitation amplitude, and consequently making them impractical for use in flight QMS sensors and unsuitable for many commercial applications. This paper describes a highly efficient technique that enables parametric excitation for spaceborne applications. Section II reviews parametric excitation techniques and discusses a new operating mode that uses an auxiliary frequency nearly twice that of the fundamental radio frequency (RF) in order to increase the dynamic range of the sensed auxiliary signal amplitude and to provide increased peak stability through operation of voltage scan lines through the center of upper stability islands. Section III introduces a multiresonant tank circuit that enables efficient driving of the quadrupole rods with these larger excitation amplitudes, as well as a field programmable gate array (FPGA)-based voltage control system that is used to manage and drive all QMS frequency components. Finally, Sec. IV presents experimental verification of the proposed techniques and describes their implications for future space missions.

II. PARAMETRIC EXCITATION

A typical spaceborne QMS sensor is composed of four parallel conducting rods of hyperbolic cross section spaced by distance r_o from the center. DC (amplitude U) and RF (amplitude V and frequency Ω) voltages are applied to opposing pairs of rods with opposite polarities. Low-energy ions, which may be recently ionized, are injected through the rods and deflected by the electric field such that only

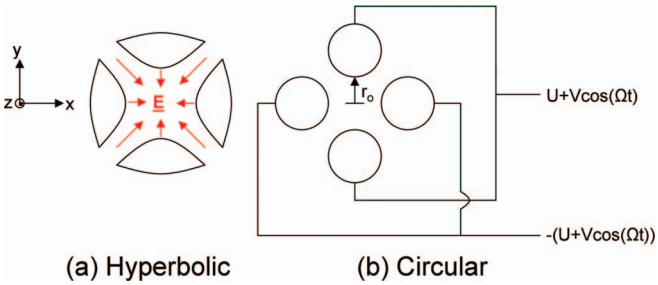

FIG. 1. (Color online) Geometry of quadrupole rods for (a) hyperbolic and (b) circular rod sensors. The potential applied to opposing pairs of quadrupole rods, $\pm(U + V\cos(\Omega t))$ is shown for the circular rods, though identical connections exist for hyperbolic geometry. Ions are injected into the rods along the $\hat{z}$ direction, and their trajectories are modified by the quadrupole electric field, $\underline{\mathbf{E}}$, in the $\hat{x}$ and $\hat{y}$ directions. The electric field for circular rod geometry mimicks that formed from hyperbolic geometry, but becomes increasingly distorted with increasing distance from the center of the rod system.

ions with a particular mass-to-charge (m/Z) ratio have stable trajectories, passing through the volume between the rods. All other ions are ejected out of that volume and are lost. Less expensive circular rods are sometimes used in commercial instruments that can produce a slightly distorted quadrupole electric field, resulting in reduced performance.[2] Although proper sizing and alignment of circular rods can help to minimize these distortions,[19] all previous spaceflight instruments have utilized hyperbolic geometry to ensure the best possible instrument performance. Figure 1 illustrates the application of combined DC and RF potentials to opposite rod pairs.

A similarity transformation can be applied to the equations of ion motion in an ideal quadrupole field to produce a set of Mathieu differential equations[2] that are written in terms of dimensionless voltages a and q and dimensionless time $\xi = \Omega t/2$, with geometry (x,y,r_o) defined in Figure 1:

$$\frac{d^2x}{d\xi^2} + (a - 2q\cos(2\xi))x = 0 \quad \text{and} \tag{1}$$

$$\frac{d^2y}{d\xi^2} - (a - 2q\cos(2\xi))y = 0, \tag{2}$$

where

$$a = \frac{8ZeU}{mr_o^2\Omega^2} \quad \text{and} \quad q = \frac{4ZeV}{mr_o^2\Omega^2}. \tag{3}$$

Here, e is the magnitude of the charge of an electron and Z is the ion charge number. m is the ion mass in units of *kilograms*, x, y, and r_o are in units of *meters*, U and V are in units of *Volts*, and Ω is in units of *rad/s*. These equations have several classes of solutions that depend on the combinations of scaled RF and DC voltage amplitudes q and a, respectively. Stable ion trajectories are periodic and bounded, allowing ions to travel through the rods unhindered. While most unstable ion trajectories will result in ions hitting the rods, never reaching the detector, some may not be ejected by the time they traverse the rod set, resulting in imperfect mass peak shapes. For constant rod geometry and operating frequencies, q and a vary only with ion m/Z, creating a set of voltages that only allow a particular range of m/Z ratios to reach the detector, i.e., in normal quadrupole operation, a

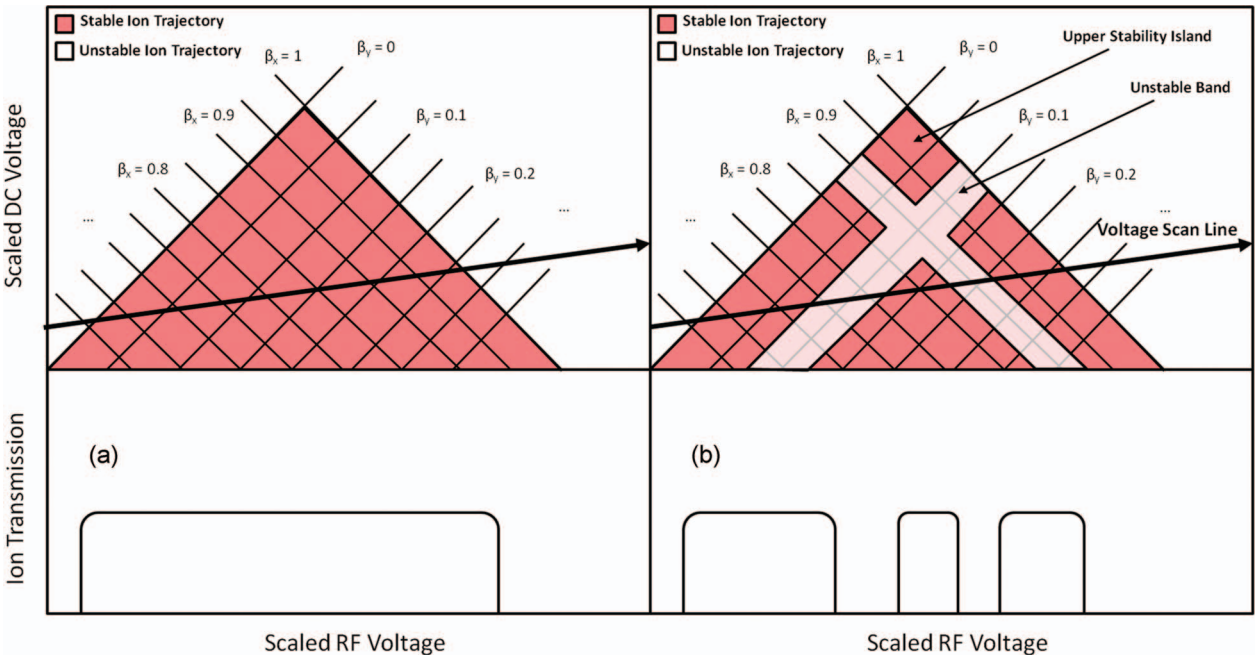

FIG. 2. (Color online) (a) **Nominal QMS operation:** Combinations of RF and DC voltage amplitudes result in either stable or unstable ion trajectories. A controlled scan line of voltages that passes through a stable region yields a mass peak. The stability region is ordered by lines of constant β_x and β_y that are parameters that correspond to frequency components of ion trajectories. (b) **Parametric excitation mode:** The insertion of additional frequency components excites parametric resonances along iso-β lines, creating bands of instability and an upper stability island.

controlled scan line of voltages that passes through a stable region yields a series of mass peaks with increasing *m*/*Z*. The slope of this scan line (λ) is frequently defined as

$$\lambda = \frac{U}{V} = \frac{a}{2q}. \tag{4}$$

The resolution (R_w) and transmission (T_w) of these mass peaks must be defined in terms of a reference value (w) that define the peak boundaries. For example, for $w = 0.10$, $R_{0.1}$ is defined as M/ΔM where M is the mass of interest and ΔM defined as the width of the mass peak with transmissions greater than 10% of the maximum transmission value. $T_{0.10}$ is defined as the average transmission of the mass peak within that same ΔM range. Results of previous work have been in terms of $w = 0.50$ (Refs. 16 and 17) and $w = 0.10$.[14,15] However, for cases where the dynamic range of measured mass peaks is of vital importance, such as for space applications, $w \leq 0.01$ are of interest.

The region of stable ion trajectories is ordered by lines of constant β_x and β_y, parameters that correspond to the frequency components of ion trajectories in the x and y coordinates, respectively. For typical stable trajectories,[2] β_x and β_y are both between 0 and 1, as shown in Figure 2(a). Driving the quadrupole rods at one of these frequencies with voltage amplitude V_{ex} excites parametric resonances.

These resonances create bands of instability in the stable region along lines of constant β, as shown in Figure 2(b). The original stability region breaks into smaller sections, including an upper stability island that was originally discussed in a patent by Miseki.[20] Since that time, the upper stability island has been the source of more in-depth analytical and experimental study.[14–17] This splitting is analogous to the normal modes of a dynamical system,[21] where an ion trajectory is modeled as a superposition of harmonic oscillators with secular frequencies related to β_x and β_y. Excitation at a given frequency can create a resonant ion trajectory, just as driving a system at one of its normal modes can result in large amplitude oscillations. The amplitude of the ion trajectory will quickly grow such that the ion strikes the QMS rods rather than reaching a detector, even if it is of the appropriate *m*/*Z* in nominal QMS operation. It has been shown through modeling that operating a QMS in the upper stability island can result in improved peak shapes and mass resolution even for ideal hyperbolic rod sensors.[15] This technique can also be used to correct for nonlinear resonances that arise naturally as a consequence of using circular rod sensors or from imperfections in the rod alignment or manufacturing processes.[16,17]

Sudakov *et al.*[18] have derived a general resonance condition that relates the parameter β and quadrupole operating frequencies. This condition can be written in terms of an excitation frequency parameter, f, the auxiliary frequency, ω_{aux}, and the fundamental RF frequency, Ω_{RF}, such that

$$f \equiv \frac{\omega_{aux}}{\Omega_{RF}}, \quad \text{and} \quad Kf = |n + \beta|. \tag{5}$$

Here, K is the order of resonance, i.e., 1, 2, 3, . . . , and n is the resonant mode number, i.e., ± 0, ± 1, ± 2, ...

This auxiliary signal will modify the ion equations of motion with

$$\frac{d^2x}{d\xi^2} + (a - 2q\cos(2\xi) - 2q'\cos(2\xi f))x = 0 \quad \text{and} \tag{6}$$

$$\frac{d^2y}{d\xi^2} - (a - 2q\cos(2\xi) - 2q'\cos(2\xi f))y = 0, \tag{7}$$

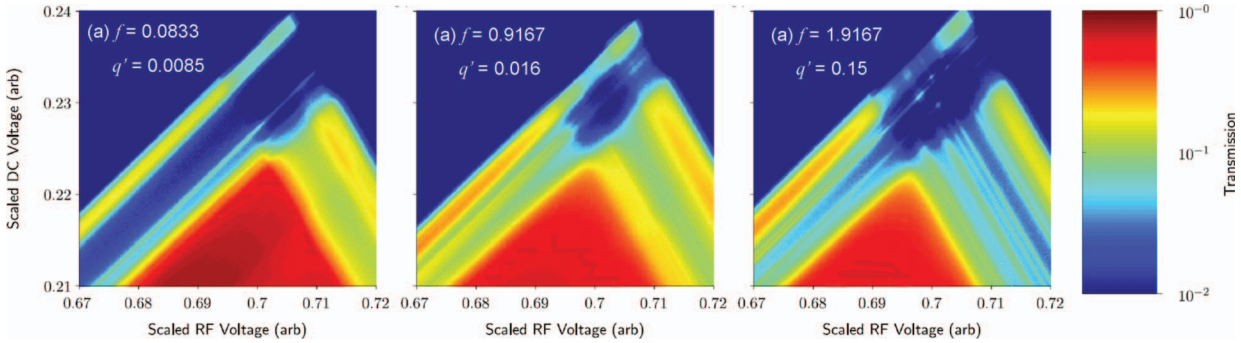

FIG. 3. (Color online) Numerically simulated quadrupole stability diagrams for (a) $f = 0.08333$, $q' = 0.0085$, (b) $f = 0.9167$, $q' = 0.016$, and (c) $f = 1.9167$, $q' = 0.15$. Ions spent 40 RF cycles traversing the quadrupole rods with an aperture of $0.232r_o$. While the stability regions for each excitation mode exhibits slightly different features, the location and size of the upper stability island are similar for each.

where

$$q' \equiv q\frac{V_{ex}}{V}. \tag{8}$$

As an example, consider a first-order resonance, $K = 1$. A single auxiliary frequency, $f = 0.9$, can yield resonances at both $\beta = 0.1$ and $\beta = 0.9$ for low mode numbers $|n| = 0$, 1. As shown in Figure 2(a), at the tip of the stability region, β_x approaches 1 and β_y approaches 0. Therefore, for parametric excitation of $f = 0.9$, the resonances along $\beta_x = 0.9$ and $\beta_y = 0.1$ will form an upper stability island, as shown in Figure 2(b).

A. Stability island operation

There are multiple ways to adjust the mass resolution when operating in an upper stability island. For a fixed island size, i.e., fixed frequency f and excitation amplitude q', the slope of the scan line λ can be adjusted such that it passes through the upper or lower tips of the island. Large ranges of mass resolution can be achieved through formation of relatively large stability islands, requiring only small excitation amplitudes to achieve the desired island splitting. This method has been the preferred mode of operation of previous work.[16,17]

Alternatively, the size of the stability island itself can be adjusted, i.e., variation of either frequency and/or excitation amplitude. The slope of the scan line is adjusted such that it passes through the center of the island, forming a mass peak having the maximum width of the island. Such operation has two advantages over operation at the island tips. First, for high-resolution modes, transmission is maximized.[15,17] Second, mass peak variability is minimized. Consider small perturbations of the slope of the scan line due to electronics or control system errors. Near the tip of a stable region, both the transmission and peak width change significantly with small changes in slope, creating potentially wildly varying peak shapes. The center of the stability island, however, is much less sensitive to errors in scan line slopes, as it is more symmetric than the island tips with respect to both changes in peak width and transmission. Operation through the center of the stability island has not previously been applied to laboratory work due to the prohibitively large excitation amplitudes required to form sufficiently small islands.

B. Higher order resonances

Consider resonances defined by Eq. (5) of a given order, i.e., fixed K. As the excitation frequency parameter f increases, the absolute value of n must increase in order to have a resonance at a particular $0 < \beta < 1$, i.e., higher frequency excitations can only cause resonances of higher order modes. The energy available for each mode drops off quickly[21] with n, so significantly more excitation energy must be added before a resonance of sufficient strength creates adequate island formation at higher frequencies. As an example, Figure 3 illustrates the required excitation to obtain similar island splitting for operating frequencies corresponding to $f = 0.0833$, $f = 0.9167$, and $f = 1.9167$, using a numerical simulation of Eqs. (6) and (7). Trajectories for 40,000 total random ions were calculated at each of 500×500 (q,a) points using a 4th order Runge-Kutta numerical scheme. Ions were axially initialized within an aperture of $0.232r_o$ ($r_o = 6.7$ *mm*) with one of 20 different initial phases. Simulated ions spent approximately 40 RF cycles in the rods to match the experimental setup used later in this paper. Fringing-field and ion energy spread effects were not taken into account.

From Figure 3, is is clear that for higher auxiliary frequencies f, higher excitation amplitudes are required. Adding more excitation energy to the system has negative connotations, as it implies increased power consumption of the QMS. However, the efficiency at which the energy is inserted into the system must be considered, as will be discussed. Furthermore, for increased q', the dynamic range of the sensed auxiliary signal amplitude is higher. The sensed amplitude is the potential difference between the quadrupole rods created by the auxiliary signal. Electronics that measure this signal as part of a closed-loop feedback system require less precision to sense larger amplitudes. Therefore, from both control system and electronics development perspectives, operation near $f = 2$ is favored.

While auxiliary excitation techniques near $f = 0$ and $f = 1$ have been experimentally verified,[16,17] a practical space-based application has not yet been achieved due to power and other technical implications of the proposed solutions. As mentioned previously, these studies operate scan lines through the upper and lower tips of stability islands. This work, however, chooses to scan voltages such that they pass through the center of formed stability islands,

simultaneously maximizing both ion transmission and mass peak shape stability, vital metrics for a spaceborne sensor, where scan integration time is held at a premium. While the island splitting from Figure 3 is similar for the $f \approx 0$, 1, and $f \approx 2$ operating frequencies, the subtle differences in island shapes and locations due to the relative strengths of resonant modes can lead to differences in instrument performance. In comparing $f \approx 0$ and $f \approx 1$ operating points, Zhao *et al.*[17] found that $f \approx 0$ yields the highest attainable mass resolution for a system, though $f \approx 1$ gave higher average transmission and still achieved relatively high resolutions. Given the limitations of electronics used for this work, we are unable to experimentally compare $f \approx 0$, 1, and $f \approx 2$ at high resolutions. However, $f \approx 2$ operation is expected to produce similar performance to the $f \approx 1$ modes tested due to their similar sets of resonant β_x and β_y values from Eq. (5).

High-resolution measurements will require the formation of smaller islands, i.e., increased excitation signal amplitude. This problem is seemingly exacerbated through the use of higher order resonant excitation, which requires significantly stronger driving amplitudes. However, as will be shown, a new multiresonant tank circuit permits the use of such amplitudes without significant increases in required driving current. The nature of this circuit necessitates operation near $f \approx 2$, which maximizes the sensed excitation amplitude and enables these technologies to be applied to the next generation of QMS space instruments.

III. IMPLEMENTATION

As mentioned previously, existing quadrupoles have already been modified to take advantage of parametric excitation near $f = 0$ and $f = 1$. These modifications have involved the direct insertion of an auxiliary signal into the quadrupole tank circuit independent of the fundamental RF waveform. The relative phases and amplitudes of each frequency component were not controlled in a precise way and are therefore currently unsuitable for integration into spaceborne QMS sensors. This section introduces a novel multiresonant tank circuit and an FPGA-based voltage control system to create a more precise implementation of auxiliary excitation techniques, and to enable the use of $f \approx 2$ higher order parametric excitations for space applications.

An operating frequency of $f = 1.9167$ is used as an example throughout this paper, since for a relatively large excitation amplitude ($q' \approx 0.15$), a sufficiently small stability island will be formed that should yield the maximum mass resolution $O(10^2)$ within the limitations of the developed electronics. Consequently, the increased transmission predicted for high-resolution modes[15] when using auxiliary excitation will not be experimentally verified in this work.

A. Typical quadrupole tank circuit

The maximum peak-to-peak voltage amplitude applied across the quadrupole rods is dependent on the desired maximum mass-to-charge ratio $(m/Z)_{max}$ in *amu/charge number*, operating frequency Ω_{RF} in *rad/s*, and rod spacing r_o in *meters*, such that V_{max} in *Volts* becomes,[2]

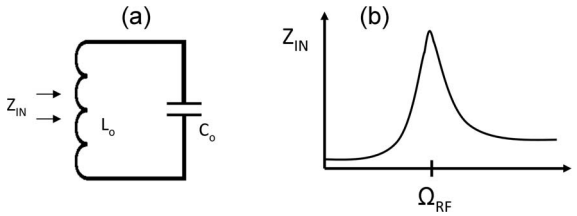

FIG. 4. Typical single pole resonant LC tank circuit. (a) Schematic and (b) corresponding input impedance.

$$V_{max} = \frac{(\Omega_{RF}/2\pi)^2 r_o^2}{7 \times 10^6} \left(\frac{m}{Z}\right)_{max}. \tag{9}$$

For practical space instruments, amplitudes of several hundred volts are required to distinguish between neighboring species with large mass-to-charge ratios. In order to produce AC voltages of these magnitudes in a power efficient way, resonant circuit techniques are employed. The quadrupole rods themselves present an almost ideal capacitance C_o. When placed in parallel with an inductance L_o (typically the secondary windings of a step-up transformer), the rods form a parallel resonant LC tank circuit with resonant frequency,

$$\Omega_{RF}^2 = \frac{1}{L_o C_o}. \tag{10}$$

The operating frequency of the QMS is therefore selected to be Ω_{RF}. Using the complex representation of the L_o and C_o components, the input impedance of this circuit (see Figure 4) can be written as

$$Z_{IN,o}(\omega) = \frac{-j\omega L_o \Omega_{RF}^2}{\omega^2 - \Omega_{RF}^2}, \tag{11}$$

where there is a single pole at $\omega = \Omega_{RF}$. In practice, $Z_{IN,o}$ will remain finite as $\omega \to \Omega_{RF}$ due to losses of inductors and capacitors used in the resonant circuit, as discussed in Appendix A 1. The sharpness of the actual resonant peak can be written in terms of the quality-factor (Q-factor) of the circuit,

$$Q \equiv \frac{\omega}{\Delta\omega}, \tag{12}$$

where ω is the resonant frequency and $\Delta\omega$ is the $-3dB$ bandwidth of the peak. For a high-Q, low-loss, resonant LC circuit, the impedance quickly drops as one moves away from the pole in frequency. Resonant circuits for quadrupole applications typically require $Q \approx 100$.

Operation at the resonant frequency has a number of advantages. First, the driving current required to create a given potential difference across the quadrupole rods is a minimum since the current required to create a particular voltage drop across the rods varies inversely proportional to Z_{IN}. Second, the driving point impedance of the LC circuit is purely real, relaxing requirements on driving circuitry and causing zero phase shift of the RF waveform.

For a single-pole resonant circuit with quality factor Q, the required driving current magnitude I (normalized to the required current of an unmodulated QMS I_o) for an auxiliary

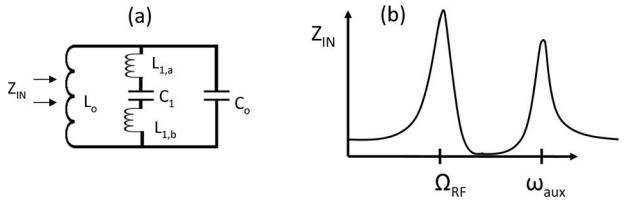

FIG. 5. Multiresonant tank circuit. (a) Schematic with added Foster-derived impedance network and (b) corresponding circuit input impedance as a function of frequency.

signal with excitation strength q' at frequency $\omega_{aux} = f\Omega_{RF}$ can be written as (see Appendix A 1 e),

$$\left|\frac{I}{I_o}\right| = 1 + q'\sqrt{1 + Q^2\left(1 - \frac{1}{f^2}\right)^2}. \tag{13}$$

Here, the fundamental frequency is driven at resonance, but the auxiliary signal is not, leading to a reduction of driving efficiency at the excitation frequency, as well as a significant phase advance of the auxiliary signal.

B. Multiresonant tank circuit

Unlike the traditional single pole tank circuit, a tank circuit that is resonant at more than one frequency enables resonances at all QMS operating frequencies. Like a single pole tank circuit, a multiresonant tank circuit should still have the quadrupole capacitance in parallel with the secondary windings of a step-up transformer. An impedance network synthesized by Foster's second form expansion[22] adds elements in parallel to the traditional LC circuit, creating an additional pole and zero. This second pole is introduced at a frequency $\omega_{aux} \approx 2\Omega_{RF}$, resulting in an impedance network that has resonant peaks at both driving frequencies. This expansion can be generalized for any number of added poles, just by adding more Foster-derived networks to the circuit. Figure 5 shows a schematic for a tank circuit with an added Foster-derived network of L_1 and C_1. Here the inductance L_1 has been split up into 2 equal halves, $L_{1,a}$ and $L_{1,b}$, so that the circuit is balanced with respect to ground.

1. Component selection

Given the schematic in Figure 5, the following frequencies are defined:

$$\omega_o^2 \equiv \frac{1}{L_o C_o} \quad \text{and} \quad \omega_1^2 \equiv \frac{1}{L_1 C_1}. \tag{14}$$

Using the complex representation of the L_o, L_1, C_o, and C_1 components, the input impedance of this circuit, Z_{IN} can be written in terms of these frequencies and component values as,

$$Z_{IN}(\omega) = \frac{-j\omega L_o(\omega^2 - \omega_1^2)\omega_o^2}{\omega^4 - \omega^2\left(\omega_1^2 + \omega_o^2\left[1 + \frac{L_o}{L_1}\right]\right) + \omega_o^2\omega_1^2}. \tag{15}$$

This circuit has one zero at $\omega = \omega_1$ and two poles (i.e., the operating frequencies) on either side of that zero, Ω_{RF} and ω_{aux}. These frequencies are related by parameters f and g defined such that f is the ratio between the two operating frequencies (Eq. (5)) and g is the location of the zero frequency relative to the two poles,

$$g \equiv \frac{\omega_{aux} - \omega_1}{\omega_{aux} - \Omega_{RF}}. \tag{16}$$

Following the derivation in Appendix A 1 a, values of components L_o, L_1, and C_1 can be determined for a desired operating point. Parameter values of $f \approx 2$ and $g \approx 0.5$ are used, yielding

$$L_o \approx \frac{0.56}{\Omega_{RF}^2 C_o}, \tag{17}$$

$$C_1 \approx 0.43 C_o, \tag{18}$$

and

$$L_1 \approx \frac{1.03}{\Omega_{RF}^2 C_o}. \tag{19}$$

From Eqs. (17)–(19), the inductance values of L_1 (split into two equal parts L_{1a} and L_{1b}) and L_o are of similar magnitudes, as are the capacitance values of C_1 and C_o. Therefore, in general, the design and component requirements of the single-resonant tank circuit apply to the capacitors and inductors used for a multiresonant tank circuit.

2. Driving current requirements

Following Appendix A 1 d, when driving the QMS at two resonant frequencies with excitation strength q', the new driving current I, normalized by I_o, can be written as

$$\left|\frac{I}{I_o}\right| \approx \frac{Z_{INo}(\Omega_{RF})}{Z_{IN}(\Omega_{RF})}\left[1 + q' \times \frac{Z_{IN}(\Omega_{RF})}{Z_{IN}(\omega_{aux})}\right]. \tag{20}$$

The ratios $Z_{INo}(\Omega_{RF})/Z_{IN}(\Omega_{RF})$ and $Z_{IN}(\Omega_{RF})/Z_{IN}(\omega_{aux})$ are functions of the tank circuit parameters f and g. For example, for an operating point of $f = 1.9167$, $g = 0.5$, and Q of 200, the required driving current becomes

$$\left|\frac{I}{I_o}\right| \approx 1.37(1 + 2.68q'). \tag{21}$$

This current can be compared to an operating point of $f = 0.9167$ for a single-pole system using Eq. (13) to yield

$$\left|\frac{I}{I_o}\right| \approx 1 + 38q'. \tag{22}$$

For example, consider two high Q tank circuits with values as described in Tables I and II. As a simplification, the self-capacitance of the inductors has been neglected.

The driving point impedance (as seen through a transformer primary, as modeled in Appendix A 1 d) for each circuit as a function of frequency has been calculated and is shown in Figure 6. The reduction in the resonant peak amplitude at the fundamental frequency is apparent, as well as the enhancement in the resonant peak at the chosen auxiliary

TABLE I. Parameters for a high Q quadrupole single-pole-resonant tank circuit.

Component(s)	Value(s)
Pole(s)	1 MHz
Inductors	$L_0 = 154\ \mu H$
Losses (Q = 200 @ 1 MHz)	$R_p = 250k\Omega$, $R_s = 1\ \Omega$
Capacitors	$C_0 = 165\ pF$
Transformer Coupling	$k = 0.5$
Transformer Primary	$L_p = 500\ nH$

frequency. Previously published operating points from Konenkov *et al.*[14] and Zhao *et al.*[16,17] are marked on Figure 6 as well as a proposed new operating point of $f = 1.9167$. For high Q resonant peaks, there is a significant decrease in required driving current in the new operating point and an increase in the dynamic range of the applied excitation amplitude. For lower Q inductors, the relative reduction in driving current will be less significant, but there is still an increase in the dynamic range of the sensed excitation signal amplitude.

Consider the island splitting illustrated in Figure 3 that results in $R_{0.10}$ on the order of 10^2. The relative driving current for each operating point is shown in Table III, using the approximate calculations of Eqs. (21) and (22), and also the simulated impedance curves shown in Figure 6. While it can be difficult to achieve both a maximum in the dynamic range of the auxiliary signal amplitude and a minimum in required driving current, an order of magnitude increase in the dynamic range is easily accessible for only a modest increase in required driving current over single-pole systems. From Table III, it can be seen that Eqs. (21) and (22) provide reasonable estimations for the required driving current for $f \approx 1$ and $f \approx 2$ operating points. These equations do not apply for $f \approx 0$ operating points since their derivation rely on the frequencies of interest being near circuit resonances.

With an appropriate selection of auxiliary frequency, higher resolution modes are accessible for approximately the same relative driving current as those that provide lower resolution measurements. Due to inherent limitations in the quality of developed electronics for this work, this paper focuses on lower mass resolution modes. However, with adequate precision of electronics, higher resolution modes should be accessible using the approach and techniques discussed here. For example, numerical simulations show that an operating point of $f = 1.95$, $q' = 0.15$ can yield a $R_{0.10}$ on the order of 10^3.

TABLE II. Parameters for a high Q quadrupole multiresonant tank circuit.

Component(s)	Value(s)
Pole(s)	1 MHz, 1.9167 MHz
Inductors	$L_0 = 154\ \mu H$, $L_{1,a} = L_{1,b} = 163\ \mu H$
Losses (Q = 200 @ 1 MHz)	$R_p = 250\ k\Omega$, $R_s = 1\ \Omega$
Capacitors	$C_0 = 95\ pF$, $C_1 = 37\ pF$
Transformer coupling	$k = 0.5$
Transformer primary	$L_p = 500\ nH$

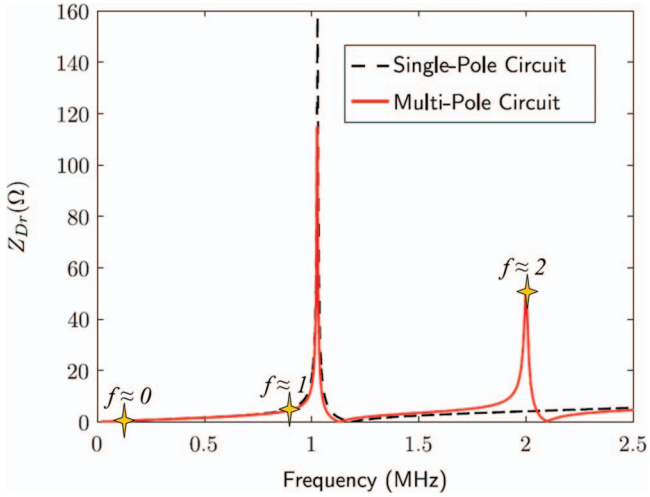

FIG. 6. (Color online) Calculated driving point impedance versus frequency for sample single-pole and multiresonant tank circuits. Experimentally verified operating points corresponding to $f \approx 0$ from Zhao *et al.*,[16,17] $f \approx 1$ from Konenkov *et al.*,[14] and $f \approx 2$ (this work), are indicated.

C. FPGA voltage control system

In order to drive a quadrupole, there must be circuitry that generates and manages all operating frequencies. In a typical single-frequency quadrupole, Ω_{RF} is synthesized through an analog oscillator and amplified to the appropriate amplitude. For multiple-frequency applications, however, the frequencies and amplitudes of multiple signals must be controlled. This complexity supports a transition from analog-based signal generation and management to a digital solution, namely a voltage control system housed in an FPGA, an integrated circuit that is composed of customizable digital logic blocks. FPGA-based control of quadrupoles has been previously studied and successfully implemented in the laboratory.[23,24] FPGA technology has also been successfully flown on spacecraft,[25] making these devices a suitable medium for development. While not a tremendous problem for terrestrial applications, the stability of the quadrupole RF source is an issue for space sensors due to the mass and power limitations of the instrument, as well as the large variations in ambient temperature that the instrument is likely to encounter. Since spaceborne quadrupole RF sources have traditionally been implemented as LC self-oscillators, their stability is a function of the stability of the employed inductances and capacitances, which must be matched to those of the resonant tank circuit. Digitally generated signals from an FPGA are more stable than their analog counterparts both in terms

TABLE III. Relative driving current requirements for simulated upper stability island QMS operating points $R_{0.10} \approx 100$. The voltage scan line for each operating point passes through the center of the formed island.

Tank Circuit	f	q'	I/I_o[a]	I/I_o[b]
Single-Pole	0.0833	0.0085	-	5.98
Single-Pole	0.9167	0.016	1.61	1.38
Multi-Pole	1.9167	0.15	1.92	1.85

[a]Calculated using Eqs. (17) and (18).
[b]Calculated from simulated driving point impedances and Eq. (16).

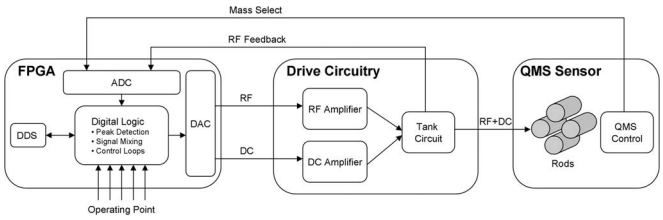

FIG. 7. Block diagram of an FPGA-based voltage control system interfaced with a QMS sensor and auxiliary electronics.

of frequency and amplitude drift, and can be dynamically adjusted to match the resonant frequencies of a tank circuit.[26]

1. System overview

Figure 7 shows a block diagram of an FPGA-based voltage control system. An FPGA-based system allows for the use of direct digital synthesis (DDS) techniques to generate all frequency components of interest. These DDS blocks generate single-frequency sinusoidal signals of the appropriate amplitude for a signal with each clock cycle. Internal to the FPGA, each frequency component can be scaled and summed together to create the final quadrupole driving waveform that is output using a digital-to-analog converter (DAC). A second DAC controls the voltage sources that provide the DC component to the quadrupole rods. Analog-to-digital converters (ADC) read a mass-select line from the quadrupole control system to determine the output voltage amplitude, as well as a feedback signal from the quadrupole rods through a capacitive divider, which contributes to the value of C_0. This signal is used to detect the amplitudes of all of the frequency components and then, along with the desired operating voltage, provides input to control loops that create a closed-loop system ensuring that the correct amplitudes for each component are properly produced. Such a feedback mechanism employing matched ceramic capacitors is commonly used in flight instruments.

IV. EXPERIMENTAL VERIFICATION AND DISCUSSION

The techniques presented can be applied to the development of completely new QMS systems, but they can also be applied to existing sensors. To experimentally verify auxiliary excitation near $f = 2$, a multiresonant tank circuit and an FPGA control system were designed to function with an existing Pfeiffer QMG422, a commercial quadrupole system. The Pfeiffer QMS has a set of 30-cm-long circular rods with 8-mm radii and an r_o spacing of 6.7 mm. As mentioned previously, most spaceborne QMS sensors use hyperbolic rods. However, for the purposes of this work, a circular rod sensor still allows one to demonstrate the proposed techniques. The tuned tank circuit (see A.1.6) yielded resonant frequencies of 1.04 MHz and 1.99 MHz, corresponding to an operating point of $f = 1.9167$, and $g \approx 0.5$. The rods are biased at a negative potential with respect to the entrance aperture to control ion energy. The rod bias was set to inject ions of approximately 10 eV. Due to limitations of the ion source used, lowering the rod bias to inject ions below ≈10eV results in significantly reduced transmission without an improvement in performance.

For the FPGA voltage control system, a Xilinx XtremeDSP Virtex 4 development kit with 14-bit ADC/DAC capabilities was interfaced to a PC with MATLAB via a PCI bus. Since only two DAC channels were available for use with this FPGA kit, a National Instrument USB-6215 device takes the output from the FPGA DAC and converts it to a DC+ and DC– control line using a LabVIEW VI. The mass select line from the Pfeiffer QMS electronics was sampled by one of the FPGA ADC channels and the Pfeiffer QMS RF control system was disabled. Auxiliary analog electronics, such as a simple class-C-like RF amplifier (see Appendix A 1 f) and high-voltage DC amplifiers, were implemented separately from any Pfeiffer QMS electronics. It should be noted that although the Pfeiffer QMG422 is specified to have unity mass resolution up to a mass of 340 amu, the tank circuit/FPGA control system was designed for masses less than 100 amu, since they were only built for experimental verification of higher order auxiliary excitation. However, extension of this system to a higher mass range could be readily accomplished through the use of higher voltage rated components.

Argon gas was ionized and injected into the quadrupole and measured using the newly created RF/DC supply for three operating points: (1) traditional operation without auxiliary excitation, (2) scanning through the tip of a large stability island formed from 10% auxiliary excitation, and (3) scanning through the center of a small stability island formed from 15% auxiliary excitation. At 10 eV, the Ar^+ ions spend approximately 40 RF cycles in the quadrupole rods. Stability diagrams created from sets of scan lines for each operating point are shown in Figures 8(a), 8(b), and 8(c). The accumulation time for each scan line was 16 ms per step, with 64 steps per amu, allowing sufficient settling time for each point. Note that this large accumulation time was a consequence of the unoptimized feedback control algorithm (see Appendix A

TABLE IV. Resolution and stability of measurements in Figure 8. Our operating mode ($q' = 0.15$) eliminates the low-mass peak tail and increases the peak stability measured at all levels by approximately a factor of ≈4 with small impact on other performance characteristics.

	$R_{0.50}$	$R_{0.10}$	$R_{0.01}$	$T_{0.50}$	$T_{0.10}$	$T_{0.01}$
$q' = 0.00$[a]	288 ± 152	129 ± 29	52 ± 13	0.026 ± 0.017	0.018 ± 0.015	0.010 ± 0.012
$q' = 0.10$[b]	274 ± 105	129 ± 21	75 ± 8	0.021 ± 0.013	0.014 ± 0.010	0.010 ± 0.008
$q' = 0.15$[c]	207 ± 99	107 ± 9	81 ± 8	0.017 ± 0.004	0.012 ± 0.003	0.009 ± 0.002

[a]Scan line through the tip of the stability region, i.e. traditional operation.
[b]Scan line operation through the tip of a stability island (Refs. 14, 16, and 17).
[c]Scan line operation through the center of a stability island.

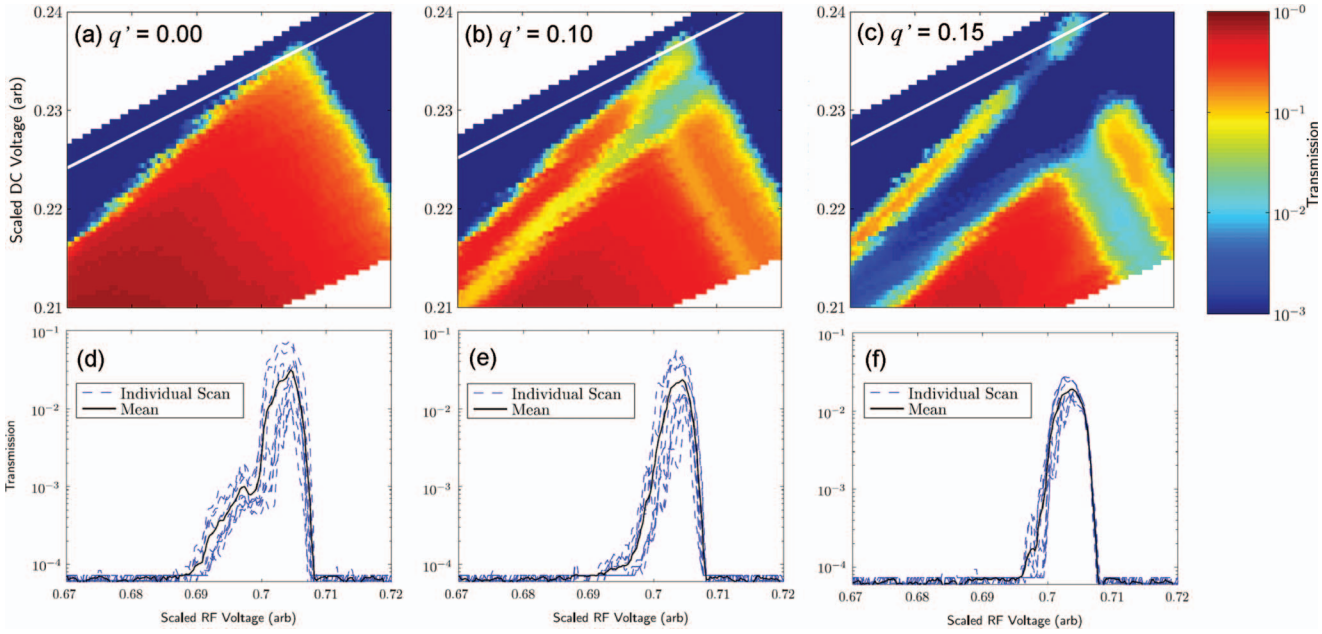

FIG. 8. (Color online) Laboratory results comparing higher order auxiliary excitation with traditional QMS operation. Measurements were performed with 10eV Ar^+ ions for (a) no auxiliary excitation ($q' = 0.00$) i.e., traditional operation, (b) $f = 1.9167$, $q' = 0.10$ auxiliary excitation analagous to previous work[14,16,17] where the scan line pass through the tip of the upper stability island, and (c) $f = 1.9167$, $q' = 0.15$ newly enabled auxiliary excitation where the scan lines pass through the center of the stability island. To measure the stability of each technique, (d),(e), and (f) show 10 successively measured mass peaks for each operating mode shown as dashed lines, with the averages appearing as solid lines. Table IV quantifies the resolution and stability of these peaks, showing that our proposed mode provides superior mass peaks.

2 c), which could in principle be significantly accelerated. Mass peaks from 10 successive scans are shown for each operating point in Figures 8(d), 8(e), and 8(f), with the mean and standard deviation of measured 50%, 10%, and 1% mass resolutions and transmission values for the 10 scans indicated for each operating point in Table IV. The slope of each scan line was selected to produce the same average transmission for each operating point.

When operating with 10% auxiliary excitation scanning through the tip of the stability island (Figure 8(e)), the low mass peak tail appearing in the traditional mode of operation (Figure 8(d)) is eliminated, resulting in an almost 50% increase in 1% mass resolution. Some of this peak tailing may be attributed to ions not spending sufficient time between the rods due to their high axial energies, but can also be a consequence of using circular rod geometry. Nevertheless, the excitation peak shapes clearly do not exhibit this feature, demonstrating an increased ejection efficiency of unwanted ions when operating with excitation, consistent with expectations. However, the variability of transmissions for each of the 10 scans is relatively unchanged from that of the non-excitation case. Following the discussion in Sec. II A, mass peaks formed from operation at the tip of any stability region will be very sensitive to errors in the scan line slope, including those formed from the tip of an upper stability island.

For operation with 15% auxiliary excitation through the center of a stability island (Figure 8(f)), the same reduction in the low mass peak tail and corresponding 50% increase in 1% mass resolution are observed. However, as discussed in Sec. II A, mass peaks created from scan lines passing through the center of an island are less sensitive to errors in scan line slope. The result is a four-fold reduction in peak variability, or conversely stated, a four-fold improvement in peak stability over the other operating modes, as calculated by the reduction in the standard deviation of measured transmissions in Table IV. This repeatability enables a more accurate computation of relative abundances of molecular species, which is vital to achieve science goals of modern planetary and cometary missions employing QMS sensors. For the same count statistical error as the unmodulated QMS, this repeatability also allows for a decreased measurement time or signal accumulation, crucial for flybys or other transient effects that require high temporal resolution measurements.

Finally, it should be noted that the measured stability regions are in good agreement with the simulations from Sec. II B in terms of the location of the expected upper stability island. The absolute transmission of ions through the QMS are necessarily different due the limitations of the simulation in terms of fringing field effects, ion entrance velocity distributions, and imperfections of the rods. The measurements do, however, show the improved peak shapes and mass resolution from operation in an upper stability island, experimentally verifying the presented techniques.

V. CONCLUSION

The presented techniques and technology are well suited for QMS sensors for space applications as they relax constraints on both the precision and power consumption of the drive electronics. Auxiliary excitation formation of an upper stability island enables QMS operating modes that boast higher mass resolution and improved peak shapes, as expected from previously discussed studies. However, implementation

of these excitation techniques is now practical. Operation near $f = 2$ results in an increase in the dynamic range of the sensed auxiliary signal amplitude, and the use of the multiresonant tank circuit enables this increase, as well as the ability to operate scan lines through the center of formed stability islands without a significant increase in driving current and power. Finally, digital synthesis of all signals allows for a more stable RF source whose operating frequencies can be dynamically adjusted in flight in response to any changes in the ambient conditions of the instrument. Such improvements enable the miniaturization of existing QMS sensors without sacrificing resolution, which could be important for various applications, such as a lander/rover-based QMS.

Furthermore, multiresonant tank circuit techniques can be generalized to any system that drives a capacitance with multiple frequencies. Therefore, in addition to the discussed applications to QMS sensors, the approach introduced in this work has the potential to lead to improved performance of quadrupole ion traps and multipole arrays. The discussed FPGA-based voltage control system can also serve to increase the stability and decrease the analog circuit complexity of such sensors.

Previous experimental work primarily used auxiliary excitation techniques to reduce peak-tailing and counteract the effect of non-linear resonances, but these two effects are more prominent in commercial circular rod sensors rather than spaceflight instruments. Nevertheless, operation in the upper stability island should still have significant advantages even for ideal hyperbolic sensors. Stable peak shapes, for example, should be a significant improvement observed for both rod geometries. For flight sensors, the use of hyperbolic rods is still necessary in order to obtain the best possible performance. A switch to circular rod geometry would lead to significant cost reduction in both the production and calibration of such instruments, if similar performance to hyperbolic rod sets could be achieved.

We have developed a thorough analysis and novel design that allows operation of QMS technology using improved peak shapes and mass resolutions with minimal impact on total power of the overall QMS design. In particular, we have shown experimentally that the QMS operation through the center of an upper stability island formed from higher order parametric excitation provides improved peak shapes, an over 50% increase in instrument 1% mass resolution, and a 400% improvement of peak stability when compared with traditional sensor operation. While not demonstrated in this work due to limitations, auxiliary excitation techniques are also expected to provide increased transmission at high resolutions when compared to a traditional ideal quadrupole. Higher frequency auxiliary excitation enables all the advantages of previously studied lower order resonant excitation, but also results in an order of magnitude increase in the dynamic range of the sensed excitation signal amplitude, and in some cases, a net savings in required driving current for similar performance. Precision control of the excitation signal and large required driving currents for $f = 0$ and $f = 1$ operating points have been prohibitive factors for feasible implementation of parametric excitation techniques in quadrupole sensors. With the introduction of $f = 2$ operating points, this paper has successfully developed and experimentally verified a method designed for the practical implementation of parametric excitation for spaceborne, and even commercial QMS applications. Using a multiresonant tank circuit and FPGA voltage control system, this method enables breakthrough science for future planetary and cometary missions using some of the oldest high-heritage measurement techniques.

ACKNOWLEDGMENTS

The authors would like to acknowledge the support of the NASA PIDDP NNX08AO05G and NASA GSRP NNX09AL50H grants that made this work possible. The University of Michigan is pursuing patent protection for the presented intellectual property and is seeking commercialization partners to help bring the technology to market.

APPENDIX: TECHNICAL APPENDIX

1. Multiresonant tank circuit design considerations

This section provides more detailed technical requirements for tank circuit components as well as an in-depth derivation of tank circuit behavior.

a. Component values

Consider the multiresonant circuit introduced in Sec. III B. The poles of this circuit occur when the denominator of Z_{IN} from Eq. (15) goes to zero such that

$$\omega_{\pm}^2 = \frac{\omega_1^2}{2}\left(1 + \frac{\omega_o^2}{\omega_1^2}\left[1 + \frac{L_o}{L_1}\right] \pm \sqrt{\left(1 + \frac{\omega_o^2}{\omega_1^2}\left[1 + \frac{L_o}{L_1}\right]\right)^2 - \frac{4\omega_o^2}{\omega_1^2}}\right), \quad \text{(A1)}$$

where

$$\omega_+ = \omega_{aux} \text{ and } \omega_- = \Omega_{RF}. \quad \text{(A2)}$$

Even with specified frequencies of operation ω_+ and ω_-, there are multiple solutions for the values of the individual components L_0, C_0, L_1, and C_1. Fortunately, the parallel capacitance C_o is bounded from below by the known capacitance of the quadrupole rods. Equations (14)-(16) can then be manipulated to solve for L_0, L_1, and C_1 in terms of the desired operating frequency Ω_{RF}, the parameters f and g, and the parallel capacitance C_o, yielding,

$$L_o = \frac{(gf + 1 - g)^2}{f^2 \Omega_{RF}^2 C_o}, \quad \text{(A3)}$$

$$C_1 = \frac{g(g-1)(g - gf - 2)(gf + f + 1 - g)(f-1)^2}{(gf + 1 - g)^4} C_o, \quad \text{(A4)}$$

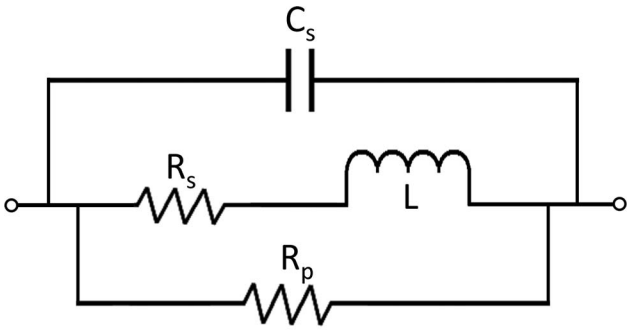

FIG. 9. Lumped element model of a non-ideal inductor with self-capacitance C_s, and series and parallel resistances R_s and R_p, respectively.

and

$$L_1 = \frac{(gf+1-g)^2}{g(g-1)(g-gf-2)(gf+f+1-g)(f-1)^2\Omega_{RF}^2 C_o}. \tag{A5}$$

b. Inductor design considerations

A non-ideal inductor can be modeled as an inductance with parallel and series resistances (R_s and R_p, respectively) and a self-capacitance (C_s), as shown in the schematic in Figure 9. The losses associated with R_p and R_s dominate the determination of Q of the circuit according to Eq. (A6), which is defined as the ratio of reactance of the inductor to its real resistance,

$$Q \approx \frac{\omega L R_p}{R_s R_p + \omega^2 L^2}. \tag{A6}$$

A high Q (>100) is required to create resonant peaks sharp enough to allow for efficient driving of the tank circuit, encouraging the use of a ferromagnetic core for L_0 and L_1. However, due to the high currents in the tank circuit, amplitude permeability and magnetic saturation effects become problematic, changing the operating point of the circuit (i.e., detuning) as a function of magnetic flux inside the cores. To synthesize an appropriate inductor, an air-gap ferrite or powdered iron core can be used that may have a reduced Q with respect to a ferrite toroid, but provide increased temperature and amplitude stability. Litz wire can be used to wind the inductors to minimize eddy current losses. With this technique, an inductor with $L \sim 10^{-4}H$, $R_p \sim 10^5\Omega$, $R_s \sim 10^0\Omega$, and $C_s \sim 10^{-12}F$ can be readily synthesized.

C_s, along with L, defines the self-resonant frequency of the core. The self capacitance of the inductor will also affect the location of the poles of the circuit. When viewed as a lump circuit, the effective inductance of the core appears as

$$L_{eff} = \frac{L}{|1-\omega^2 L C_s|}. \tag{A7}$$

For proper operation, the self-capacitance should be well above the operating frequencies, leading to $L_{eff} > L$, creating an effective boost in inductance for a given wound core.

c. Maximum current through components

The driving current through a tank circuit is determined from the input impedance of the synthesized network. At resonance, this driving current is minimal. However, the peak current through each of the individual components of the tank circuit can be larger than the driving current. The currents through each of the components for a given quadrupole voltage are dominated by the ideal reactive impedances, such that for operation near $f = 2$, and $g = 1/2$, the maximum currents through the tank circuit components are

$$I_{max,L_1,C_1} \approx \frac{\Omega_{RF}^2 C_1}{|1-\Omega_{RF}^2 L_1 C_1|} V_{max} \approx 0.77\Omega_{RF} C_o V_{max}, \tag{A8}$$

$$I_{max,L_o} \approx \frac{V_{max}}{\Omega_{RF} L_o} \approx 1.78\Omega_{RF} C_o V_{max}, \tag{A9}$$

and

$$I_{max,C_o} \approx \Omega_{RF} C_o V_{max}. \tag{A10}$$

Fortunately, for $f \approx 2$ operating points, the currents in the new components L_1 and C_1 are of the same order, and in fact smaller than, those of L_0 and C_0. From Eqs. (A3)–(A5), the values of L_1 and C_1 are also expected to be smaller than those of L_0 and C_0, respectively. Therefore, similar requirements on the construction of such components should apply.

d. Relative impedance at resonance

Rewriting the input impedance of Eq. (11) in terms of factored pole frequencies, ω_+ and ω_- yields,

$$Z_{IN}(\omega) = \frac{-j\omega L_o(\omega^2-\omega_1^2)\omega_o^2}{(\omega^2-\omega_+^2)(\omega^2-\omega_-^2)}. \tag{A11}$$

The relative amplitudes of Z_{IN} at the resonant frequencies depend on the parameters f and g. Assuming Z_{IN} diverges similarly for $\omega \to \omega_+$ and $\omega \to \omega_-$, the ratio of Z_{IN} at the poles becomes,

$$\frac{Z_{IN}(\omega_-)}{Z_{IN}(\omega_+)} \sim \frac{\omega_-(\omega_1^2-\omega_-^2)}{\omega_+(\omega_+^2-\omega_1^2)} = \frac{(gf+2-g)gf^2}{(1-g)(gf-g+1+f)}. \tag{A12}$$

For $f \approx 2$, the parameter g can be written in terms of the desired relative amplitudes of Z_{IN} at the poles such that,

$$g \approx 2\sqrt{\frac{\frac{Z_{IN}(\omega_-)}{Z_{IN}(\omega_+)}+1}{\frac{Z_{IN}(\omega_-)}{Z_{IN}(\omega_+)}+4}} - 1. \tag{A13}$$

For $Z_{IN}(\omega_-)/Z_{IN}(\omega_+) = 1$, i.e., two resonances having similar amplitudes, Eq. (A13) gives $g \approx 1/4$.

In a similar manner to Eq. (A12), the relative amplitudes of the single-pole tank circuit impedance $Z_{IN,o}$ and multiresonant tank circuit impedance Z_{IN} can be computed in terms of

parameters f and g to yield,

$$\frac{Z_{IN,o}(\Omega_{RF})}{Z_{IN}(\Omega_{RF})} \sim \frac{(gf+1-g)^2(f+1)}{(gf+2-g)gf^2}. \quad \text{(A14)}$$

Note that Eqs. (A12) and (A14) are only approximations since they do not include the effects of finite Q inductors on input impedance. These equations do, however, to first order, illustrate the relative behavior of these circuits with changes in f and g.

e. Driving current requirements

For $f \approx 2$ there can be a significant reduction in the driving point impedance at the fundamental RF resonant frequency as a consequence of adding new poles and zeros into the impedance network. This reduction directly translates into the current required to drive the rods with a particular voltage. For higher frequency separation between the two poles (i.e., $f > 2$), this reduction is eliminated, but the amount of excitation needed to produce a given island splitting significantly increases.

In order to mitigate this effect, the circuit zero can be shifted toward higher frequencies at the expense of the auxiliary signal resonant peak amplitude. Note that when adding a Foster-derived network to an existing resonant circuit, the location of the fundamental RF frequency shifts to lower frequencies, so in comparing driving current, one must compare the driving point impedance of a circuit whose operating frequencies are the same, i.e., a circuit with a Foster-derived network must be compared to a single-pole circuit with additional parallel capacitance sufficient to push the pole to a lower frequency.

The reduced driving point impedance at the fundamental RF frequency can be balanced by the tremendous increase in driving point impedance at the auxiliary frequency. For example, for a single-pole high-Q circuit, the auxiliary frequency is relatively far from the resonant peak, resulting in a driving point impedance reduction by over 90%. For a high-Q multiresonant tank circuit, the driving point impedance at both the fundamental and auxiliary frequencies are comparable in magnitude.

The driving point impedance of the tank circuit dictates the driving current requirements to produce a particular potential difference across the quadrupole rods. For a traditional quadrupole operating at a given frequency $\Omega_{RF}^2 = 1/[L_0C_0]$, the current required, I_o, is inversely proportional to Z_{Dro}, the driving point impedance of a single-pole tank circuit. The driving point impedance is close to, but not exactly the same as Z_{IN}. The driving circuitry sees the tank circuit impedance reflected across the primary inductance, L_p, with coupling coefficient k. Using the circuit model of a transformer shown in Figure 10, the driving point impedance is

$$Z_{Dr} = j\omega(1-k^2)L_p + k^2 L_p Z_{IN}. \quad \text{(A15)}$$

Note that the locations of the poles of Z_{Dr} will be identical to those of Z_{IN}, but the location of the zeros will be shifted based on the coupling coefficient k and the inductance L_p.

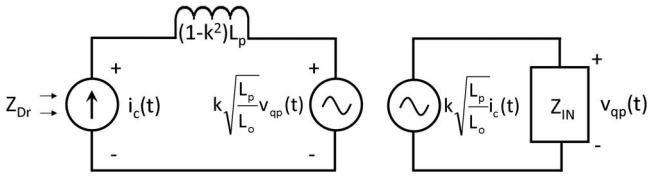

FIG. 10. Model of an inductor with coupling coefficient k, primary inductance L_p, and secondary inductance L_o. Z_{Dr} is the measured driving point impedance of the circuit. Z_{IN} is the impedance of the tank circuit network, including the secondary inductance L_o, quadrupole rod capacitance C_o, and any Foster-derived impedance networks.

Near resonances, the second term in Eq. (A15) dominates, so $Z_{Dr} \propto Z_{IN}$, enabling the use of the ratios from Eqs. (A12) and (A14) when calculating I. When driving the quadrupole at two frequencies with excitation strength q', the new driving current I, normalized by I_o, can be written as

$$\left(\frac{I}{I_o}\right) = \frac{Z_{Dro}(\Omega_{RF})}{Z_{Dr}(\Omega_{RF})}\left[1 + q' \times \frac{Z_{Dr}(\omega_-)}{Z_{Dr}(\omega_+)}\right] \approx \frac{Z_{INo}(\Omega_{RF})}{Z_{IN}(\Omega_{RF})}\left[1 + q' \times \frac{Z_{IN}(\omega_-)}{Z_{IN}(\omega_+)}\right]. \quad \text{(A16)}$$

The relative current I/I_o becomes a function of the pole-zero spacing parameters f and g, and the excitation strength q'. For $f = 2$, Figure 11 illustrates how g can be selected in order to minimize I/I_o for a given value of q'. For $q' \approx 0.1$, $g \approx 1/2$ is obtained.

For comparison, the transfer function $H_o(s)$ of a single-pole high-Q tank circuit (adapted from the general transfer function of a 2nd order bandpass filter[27]) varies as

$$H_o(s) = \frac{H_o s\Delta\omega}{s^2 + s\Delta\omega + \Omega_{RF}^2}, \quad \text{(A17)}$$

where $s \equiv j\omega$ and H_o is the maximum amplitude of the transfer function. Taking the magnitude of Eq. (A17) and using the definition of Q from Eq. (A6) yields the relative input

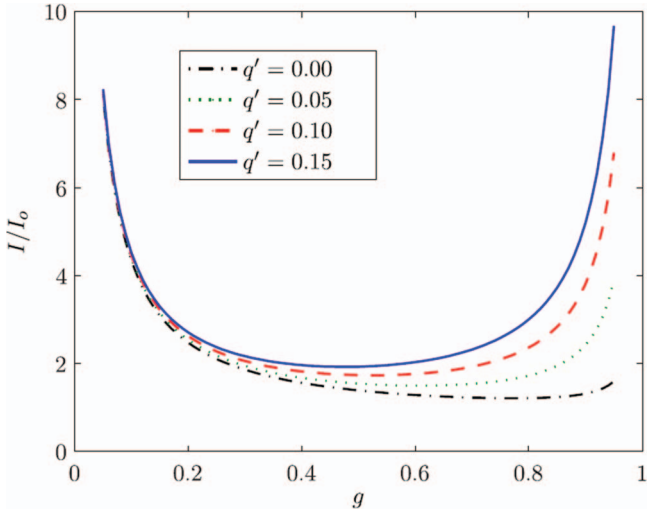

FIG. 11. (Color online) Calculated relative driving current as a function of modulation strength q' and pole-zero spacing parameter g for $f = 2$. As the excitation strength q' is increased, the value of g for which the driving current is a minimum decreases.

impedance of a single-pole tank circuit at Ω_{RF} and ω_{aux},

$$\frac{|H_o(s=j\omega_{aux})|}{|H_o(s=j\Omega_{RF})|}=\frac{Z_{IN,o}(\omega_{aux})}{Z_{IN,o}(\Omega_{RF})}=\frac{1}{\sqrt{1+Q^2(1-\frac{1}{f^2})^2}}. \tag{A18}$$

Equations (A16) and (A18) can then be combined to give the relative driving current required for a single-pole tank circuit with excitation strength q',

$$\left(\frac{I}{I_o}\right)=1+q'\sqrt{1+Q^2(1-\frac{1}{f^2})^2}. \tag{A19}$$

f. Tank circuit implementation and tuning

Tuning a physically realized multiresonant tank circuit can be nontrivial due to stray reactance in the circuit. Even if circuit components are synthesized with precise values from Eqs. (A3)–(A5), the tank circuit will not be properly tuned. Stray inductances and capacitances in the circuit will slightly shift pole and zero locations. It is therefore important to measure the operating point of the circuit in such a way that the act of measuring the locations of the resonances does not detune the network. The developed system interface already has a feedback mechanism that allows the FPGA to measure the voltage across the quadrupole rods. By sweeping the frequency applied to the rods and using this feedback signal, the locations of the poles can be measured and adjusted in the network's flight configuration.

A transformer was constructed and integrated into the impedance network, including the quadrupole rods, creating a single-pole resonant circuit. By adding known amounts of parallel capacitance to C_0 and measuring the location of the pole frequency (Ω_o), the effective inductance $L_{o,\,eff}$ can be determined, as well as the total C_0. Following Eq. (10), there should be a linear relationship between $1/\Omega_o^2$ and $C_{0,\,known}$, such that

$$\frac{1}{\Omega_o^2}=L_{o,eff}(C_{o,known}+C_{o,unknown}). \tag{A20}$$

This relationship is shown to hold in Figure 12 for a measured network. Originally, an operating point of f=1.9167, g = 0.5, and $\Omega_{RF}=2\pi\times 1$ MHz was desired for 80-pF rods. Following Eqs. (A3)–(A5) (and allowing for some additional parallel capacitance), a transformer with secondary inductance of $153\mu H$ was created. However, from Figure 12, it is clear that the effective inductance of the transformer in the full tank circuit is about 20% less than that of the measured secondary at $153\mu H$. Instead of rewinding the secondary coil to add more turns, this transformer can be used to achieve the desired operating point, but at a slightly higher frequency.

The L_1 inductors were constructed close to the desired L_1/L_0 ratio, taking into account the measured value of $L_{o,\,eff}$. L_1, a and L_1, b were constructed with values of 135 μH and 136 μH, respectively. The fully measured characteristics of each inductor can be found in Table V.

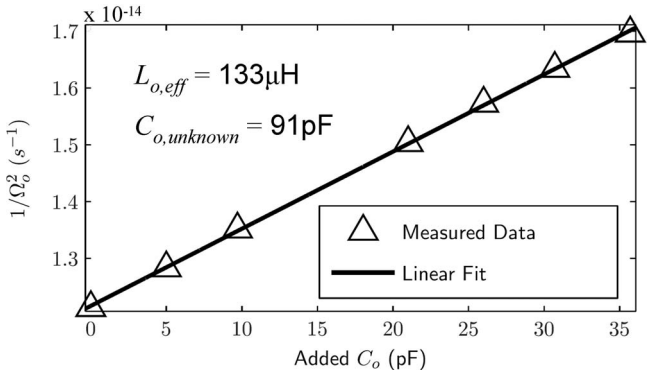

FIG. 12. $1/\Omega_o^2$ vs. added parallel capacitance C_o for a measured single-pole tank circuit.

After integrating the L_1 inductors into the tank circuit, the capacitance C_1 can be adjusted to sweep through operating points. The measured locations of the poles can be readily used to compute the value of f. However, the determination of parameter g is not as trivial. The location of the measured Z_{Dr} zeros will be shifted from that of Z_{IN} due to a non-unity coupling coefficient between the transformer primary and secondary windings. Furthermore, by measuring the circuit response through a voltage feedback signal, the precise location of the circuit zero is difficult to measure directly. However, the measurement of the change in pole locations is sufficient to recover the operating parameter g. Consider the term $\omega_1^2\omega_o^2\equiv 1/[L_oC_oL_1C_1]$. Using Eqs. (A3)–(A5), rearranging this product and solving for the zero frequency yields

$$\omega_1=\frac{\omega_{aux}\Omega_{RF}}{\omega_o}, \tag{A21}$$

where ω_o is measured during the first part of the tuning process before the Foster-derived network was added to the tank circuit, and ω_{aux} and Ω_{RF} are the measured pole locations with changing C_1. Figure 13 shows measured parameters f and g for the implemented tank circuit as a function of a known added C_1. Note that the total C_1capacitance and effective L_1 inductance can be recovered in a similar fashion to $L_{o,\,eff}$ and total C_o.

For a total C_0 of approximately 100 pF and a total C_1 value of approximately 38 pF, a desired operating point is achieved with frequencies of 1.04 MHz and 1.99 MHz, a frequency spacing parameter of $f\approx 1.9167$, and a zero location parameter of $g\approx 0.5$. As demonstrated, while it can be dif-

TABLE V. Measured properties of multiresonant tank circuit inductors.

	L_0	L_1, a	L_1, b
Core Type	PI-157-7	PI-157-10	PI-157-10
Number of windings	53-53	87	87
Wire	40-44 Litz	40-44 Litz	40-44 Litz
L	153 uH	136	135 uH
C_p	4.8 pF	1.1 pF	1.1 pF
R_p	874 $k\Omega$	330 $k\Omega$	276 $k\Omega$
R_s	1.4 Ω	1.2 Ω	1.5 Ω
Q (1 MHz)	408	241	203

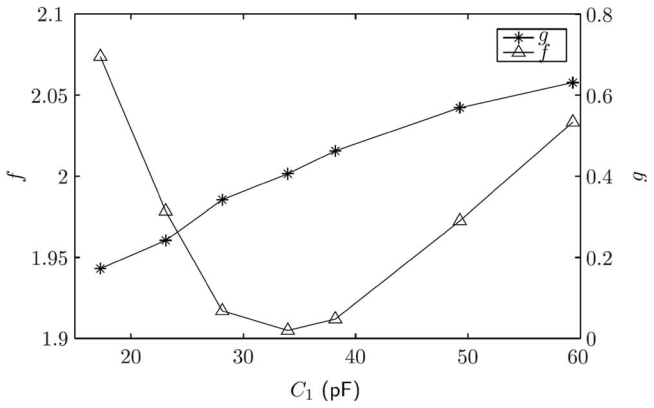

FIG. 13. Operating parameters f and g vs. Foster-derived network capacitance for a multiresonant tank circuit.

ficult to precisely match all component values, it is certainly possible to achieve an acceptable operating point. Once tuned, small, slow drifts in operating point over time can be tolerated as long as the location of the resonant peaks are known and the strength of the auxiliary signal can be adjusted accordingly.

g. Driving circuitry considerations

A simple and efficient method of driving the tank circuit is a voltage-controlled current source, for example a bipolar transistor biased to operate as a class C-like amplifier. The current waveform is shown in Figure 14, along with its corresponding frequency spectrum. This rectification, as well as any other distortion in the signal (from D/A quantization, for example), creates harmonics of the fundamental RF frequency. The high-Q tank circuit normally filters out these harmonics to create a pure, clean signal across the rods. However, with an additional pole near $2\Omega_{RF}$, there is a risk that some of this distortion will appear across the transformer secondary. Therefore, care should be taken in selection of a system operating point to avoid significant signal distortion at harmonics of the fundamental frequency affecting the stability island formation and, consequently, quadrupole performance.

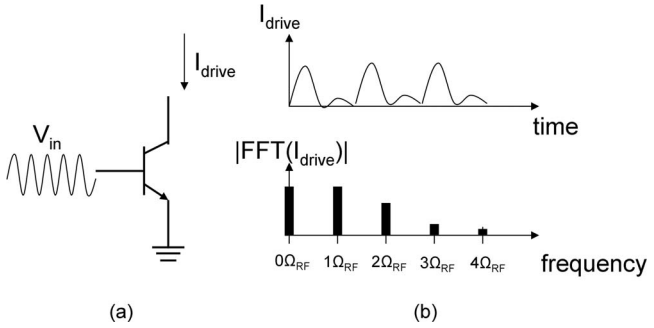

FIG. 14. (a) Sample schematic of voltage-controlled current source biased for class C-like operation. (b) Clipped current waveform at the output of the amplifier with corresponding frequency spectrum.

2. FPGA design considerations

This section provides more detailed information about FPGA design and algorithm development.

a. Synthesis of frequency components

An FPGA has a single frequency reference clock, typically on the order of 100 MHz. Direct digital synthesis (DDS) is a method of creating an arbitrary waveform from this clock, as opposed to the utilization of one or more crystal oscillators or tank circuits. For a given frequency, each clock cycle corresponds to an accumulation of phase. At each cycle, a digital word is generated from a sine wave phase-amplitude look-up table.[28] The necessary frequencies for quadrupole applications are on the order of a few MHz, providing at least a few dozen samples per cycle. A DDS block for each frequency component can be used and the output digital words can be scaled, combined, and output to a digital-to-analog converter (DAC) .

b. Detection of frequency components

The auxiliary waveform serves to modulate the envelope of the fundamental RF signal. The frequency of this modulation can be written in terms of the number of corresponding RF cycles according to Eq. (46) (for $1.5 < f < 2$),

$$\#\,\text{RF cycles} = \frac{1}{2-f}. \tag{A22}$$

For example, for $f = 1.9167$, 12 RF cycles are required to modulate the envelope of the signal one period (i.e., $\approx$0.012 ms for a 1-MHz fundamental frequency). There are a number of different methods available that can be used to sense the amplitudes of driving frequency components, in both analog and digital realms. For example, Fast Fourier transforms (FFT) or general filter-based amplitude demodulation techniques can be applied. However, to maximize detection speed and to take advantage of the known operating frequencies and low-modulation indices, a simple envelope detection technique has been implemented.

For $1/(2-f) \gg 1$, the envelope of the quadrupole signal changes slowly with respect to subsequent zero crossings. For relatively low levels of modulation ($q' \sim 0.1$), the time between zero crossings are relatively unchanged from the unmodulated signal. Let t_n and t_{n+1} be the times of two adjacent zero crossings of the measured signal. Integrating over the absolute value of the waveform between these two time steps should yield a number proportional to the signal envelope, i.e.,

$$\int_{t_n}^{t_{n+1}} |V\cos(\Omega_{RF}t) + q'V\cos(\omega_{aux}t)|dt \approx \frac{2}{\pi}\left(V + q'V\cos\left(\Omega_{RF}(2-f)\frac{t_n+t_{n+1}}{2}\right)\right)\Delta t_{n,n+1}, \tag{A23}$$

where $\Delta t_{n,\,n+1} \equiv t_{n+1} - t_n$.

The integral in Eq. (A23) generates one number every FPGA clock cycle. Values corresponding to intermediate clock cycles can be computed through linear interpolation, which serves to reconstruct the envelope signal, $V + q'V\cos(\Omega_{RF}(2 - f)t)$ for all cycles. Integrating this signal over a full envelope period, accumulating positive and negative signal sectors separately, gives a number proportional to V. Integrating the derivative of the envelope signal gives a number proportional to $q'V$. These proportionality constants will be frequency dependent. However, for fixed frequency operation, these constants can be determined through calibration, resulting in the measured amplitudes of the fundamental RF frequency (V) and the auxiliary signal ($q'V$).

This envelope detection algorithm can be implemented using only addition and fixed point multiplication operations, ideal for FPGA applications. No phase-locked loops or additional digital filters are needed, only a zero-crossing detector. For 10 measured periods of the envelope signal and $f = 1.9167$, the total data acquisition time would be approximately 0.12 ms.

c. PID control loops

A proportional-integral-derivative (PID) controller is a closed-loop feedback control scheme.[29] An error signal between the measured (through a feedback signal) and desired rod voltage is calculated. The error signal (e(t)) is scaled (P), integrated (I), differentiated (D), and then applied to the rods as the amplitude V(t) in Eq. (A24). Over several time steps, if the controller is properly tuned (i.e., appropriate coefficients K_p, K_i, and K_d are selected), the measured set-point approaches the desired one,

$$V(t) = K_p e(t) + K_i \int_0^t e(\tau)d\tau + K_d \frac{d}{dt} e(t). \qquad \text{(A24)}$$

The total settling time of the closed loop will depend on several factors. First, a sufficient sample of the feedback signal must be digitally acquired and the amplitudes of frequency components must be determined. The PID control outputs are updated with the latest error signal and a new output waveform is applied to the rods. A characteristic settling time will be required before the signal should be resampled. That settling time will be controlled by the bandwidth of the tank circuit (Q ≈200 @ 1 MHz) such that

$$\Delta t_{settle} = \frac{2\pi Q}{\Omega_{RF}} \approx 0.2 \text{ ms}. \qquad \text{(A25)}$$

Combined with an acquisition time of 0.12 ms, the total open loop settling time will be less than 1 ms. The closed loop settling time will be determined by the number of steps the controller takes to reach its nominal value. For this simple application, the basic PID loop settling time was tuned to about 20 steps. However, more sophisticated feedback techniques, such as adding a feed-forward component to the existing PID controller, could potentially serve to significantly reduce the required settling time. Since the amplitude of the excitation signal is proportional to that of the fundamental RF waveform, the auxiliary PID loop will necessarily converge after the settling of the main PID loop.

[1] W. Paul and H. Steinwedel, Z. Naturforsch., A: J. Phys. Sci. **8**(7), 448 (1953).
[2] P. H. Dawson, in *Quadrupole Mass Spectrometry and Its Applications*, edited by Peter H. Dawson (Elsevier, New York, 1976).
[3] J. H. Waite, W. S. Lewis, W. T. Kasprzak, V. G. Anicich, B. P. Block, T. E. Cravens, G. G. Fletcher, W. H. Ip, J. G. Luhmann, R. L. Mcnutt, H. B. Niemann, J. K. Parejko, J. E. Richards, R. L. Thorpe, E. M. Walter, and R. V. Yelle, Space Sci. Rev. **114**, 113 (2004).
[4] H. B. Niemann, D. N. Harpold, S. K. Atreya, G. R. Carignan, D. M. Hunten, and T. C. Owen, Space Sci. Rev. **60**, 111 (1992).
[5] H. B. Niemann, J. R. Booth, J. E. Cooley, R. E. Hartle, W. T. Kasprzak, N. W. Spencer, S. H. Way, D. M. Hunten, and G. R. Carignan, IEEE Trans. Geosci. Remote Sens. **18**, 60 (1980).
[6] H. B. Niemann, S. Atreya, S. J. Bauer, K. Biemann, B. Block, G. Carignan, T. Donahue, L. Frost, D. Gautier, D. Harpold, D. Hunten, G. Israel, J. Lunine, K. Mauersberger, T. Owen, F. Raulin, J. Richards, and S. Way, "The Gas Chromatograph Mass Spectrometer Aboard Huygens," in *Huygens: Science, Payload and Mission* edited by A. Wilson (ESA, Paris, 1997), p. 85.
[7] J. I. Lunine, Proc. Natl. Acad. Sci. U.S.A. **98**, 809 (2001).
[8] J. Geiss and G. Gloeckler, Space Sci. Rev. **106**, 3 (2003).
[9] P. R. Mahaffy, T. M. Donahue, S. K. Atreya, T. C. Owen, and H. B. Niemann, Space Sci. Rev. **84**, 251 (1998).
[10] P. R. Mahaffy, H. B. Niemann, A. Alpert, S. K. Atreya, J. Demick, T. M. Donahue, D. N. Harpold, and T. C. Owen, J. Geophys. Res. **105**, 15061, doi:10.1029/1999JE001224 (2000).
[11] M. J S. Belton, *New Frontiers in the Solar System - An Integrated Exploration Strategy* (The National Academies, Washington DC, 2003).
[12] R. E. March and J. F. J. Todd, *Quadrupole Ion Trap Mass Spectrometry* (John Wiley and Sons, Inc., Hoboken, NJ, 2005).
[13] G. Devant, P. Fercocq, G. Lepetit, and O. Maulat, Procede d'alimentation en tension des spectrographs de mass du type quadripolaire, French patent 2,620,568 (1989).
[14] N. V. Konenkov, L. M. Cousins, V. I. Baranov, and M. Yu. Sudakov, Int. J. Mass Spectrom. **208**, 17 (2001).
[15] N. Konenkov, A. Korolkov, and M. Machmudov, J. Am. Soc. Mass Spectrom. **16**, 379 (2005).
[16] X. Zhao, Z. Xiao, and D. J. Douglas, Anal. Chem. **81**, 5806 (2009).
[17] X. Zhao, Z. Xiao, and D. J. Douglas, J. Am. Soc. Mass Spectrom. **21**(3), 393 (2010).
[18] M. Sudakov, N. Konenkov, D. J. Douglas, and T. Glebova, J. Am. Soc. Mass Spectrom. **11**, 10 (2000).
[19] D. J. Douglas and N. V. Konenkov, Rapid Commun. Mass Spectrom. **16**, 1425 (2002).
[20] K. Miseki, Quadrupole mass spectrometer, US. patent 5,227,629 (1993).
[21] R. L. Alfred, F. A. Londry, and R. E. March, Int. J. Mass Spectrom. Ion Process. **125**, 171 (1993).
[22] R. M. Foster, Bell Syst. Tech. J. **3**, 259 (1924).
[23] Y. Jiang, X. Fang, Y. Rang, and D. Tian, Chin. J. Anal. Chem. **36**, 715 (2008).
[24] R. T. Schaefer, J. A. MacAskill, M. Mojarradi, A. Chutjian, M. R. Darrach, S. M. Madzunkov, and B. J. Shortt, Rev. Sci. Instrum. **79**, 095107 (2008).
[25] D. J. Mabry, S. J. Hansel, and J. B. Blake, IEEE Trans. Geosci. Remote Sens. **31**, 572 (1993).
[26] J. Vankka and K. Halonen, *Direct Digital Synthesizers: Theory, Design, and Applications* (Kluwer Academic, Boston, 2001).
[27] B. A. Shenoi, *Introduction to Digital Signal Processing and Filter Design* (Wiley-Interscience, New York, 2005).
[28] J. Tierney, C. Rader, and B. Gold, IEEE Trans. Audio Electroacoust. **19**, 48 (1971).
[29] S. Bennett, *A History of Control Engineering 1930-1955* (Peter Peregrinus, London, 1993).